





## Article

# Photocatalytic and Electrocatalytic Properties of Cu-Loaded ZIF-67-Derivatized Bean Sprout-Like Co-TiO<sub>2</sub>/Ti Nanostructures

Hye Ji Jang<sup>1,2</sup>, So Jeong Park<sup>1</sup>, Ju Hyun Yang<sup>1,2</sup>, Sung-Min Hong<sup>1,2</sup>, Choong Kyun Rhee<sup>1</sup>   
and Youngku Sohn<sup>1,2,\*</sup> 

<sup>1</sup> Department of Chemistry, Chungnam National University, Daejeon 34134, Korea; gpwldndud@naver.com (H.J.J.); jsjs5921@naver.com (S.J.P.); mil03076@naver.com (J.H.Y.); qwqe212@naver.com (S.-M.H.); ckrhee@cnu.ac.kr (C.K.R.)

<sup>2</sup> Department of Chemical Engineering and Applied Chemistry, Chungnam National University, Daejeon 34134, Korea

\* Correspondence: youngkusohn@cnu.ac.kr; Tel.: +82-(42)-8216548

**Abstract:** ZIF-derivatized catalysts have shown high potential in catalysis. Herein, bean sprout-like Co-TiO<sub>2</sub>/Ti nanostructures were first synthesized by thermal treatment at 800 °C under Ar-flow conditions using sacrificial ZIF-67 templated on Ti sheets. It was observed that ZIF-67 on Ti sheets started to thermally decompose at around 350 °C and was converted to the cubic phase Co<sub>3</sub>O<sub>4</sub>. The head of the bean sprout structure was observed to be Co<sub>3</sub>O<sub>4</sub>, while the stem showed a crystal structure of rutile TiO<sub>2</sub> grown from the metallic Ti support. Cu sputter-deposited Co-TiO<sub>2</sub>/Ti nanostructures were also prepared for photocatalytic and electrocatalytic CO<sub>2</sub> reduction performances, as well as electrochemical oxygen reaction (OER). Gas chromatography results after photocatalytic CO<sub>2</sub> reduction showed that CH<sub>3</sub>OH, CO and CH<sub>4</sub> were produced as major products with the highest MeOH selectivity of 64% and minor C<sub>2</sub> compounds of C<sub>2</sub>H<sub>2</sub>, C<sub>2</sub>H<sub>4</sub> and C<sub>2</sub>H<sub>6</sub>. For electrocatalytic CO<sub>2</sub> reduction, CO, CH<sub>4</sub> and C<sub>2</sub>H<sub>4</sub> were meaningfully detected, but H<sub>2</sub> was dominantly produced. The amounts were observed to be dependent on the Cu deposition amount. Electrochemical OER performances in 0.1 M KOH electrolyte exhibited onset overpotentials of 330–430 mV (vs. RHE) and Tafel slopes of 117–134 mV/dec that were dependent on Cu-loading thickness. The present unique results provide useful information for synthesis of bean sprout-like Co-TiO<sub>2</sub>/Ti hybrid nanostructures and their applications to CO<sub>2</sub> reduction and electrochemical water splitting in energy and environmental fields.



**Citation:** Jang, H.J.; Park, S.J.; Yang, J.H.; Hong, S.-M.; Rhee, C.K.; Sohn, Y. Photocatalytic and Electrocatalytic Properties of Cu-Loaded ZIF-67-Derivatized Bean Sprout-Like Co-TiO<sub>2</sub>/Ti Nanostructures. *Nanomaterials* **2021**, *11*, 1904. <https://doi.org/10.3390/nano11081904>

Academic Editor: Giuseppe Marci

Received: 5 July 2021

Accepted: 22 July 2021

Published: 24 July 2021

**Publisher's Note:** MDPI stays neutral with regard to jurisdictional claims in published maps and institutional affiliations.



**Copyright:** © 2021 by the authors. Licensee MDPI, Basel, Switzerland. This article is an open access article distributed under the terms and conditions of the Creative Commons Attribution (CC BY) license (<https://creativecommons.org/licenses/by/4.0/>).

**Keywords:** ZIF-67; Co-TiO<sub>2</sub>/Ti; photocatalytic CO<sub>2</sub> reduction; electrocatalytic CO<sub>2</sub> reduction; oxygen evolution reaction; water splitting

## 1. Introduction

Metal–organic frameworks (MOFs) including other materials have been extensively employed in diverse application areas such as environments, adsorbents, organic light emitting displays, sensors and catalysts [1–10]. Among diverse MOFs, the zeolitic imidazolate framework (ZIF) exhibits zeolite-like topologies where imidazolate linkers are connected with tetrahedrally coordinated transition metal ions such as Co and Zn [1–27]. In this ZIF-class, ZIF-67 has Co-N tetrahedral coordination commonly synthesized with Co(II) precursor and 2-methylimidazole [5–10]. Many catalyst materials have been synthesized using ZIF-67 and examined in diverse areas of hydrogen evolution reaction (HER), oxygen evolution reaction (OER), oxygen reduction reaction (ORR), CO<sub>2</sub> hydrogenation reaction, energy storage and toluene oxidation [11–20]. For a synthetic strategy of Co<sub>3</sub>O<sub>4</sub>@TiO<sub>2</sub> composite, thermal decomposition of ZIF-67 followed by the liquid-phase deposition method was introduced [11]. The catalyst showed an overpotential of 269 mV at 10 mA cm<sup>−2</sup> and a Tafel slope of 106 mV/dec for OER test in 2 M KOH electrolyte, and an overpotential of 153 mV

and a Tafel slope of 81 mV/dec in HER test, respectively. Salahuddin et al. prepared nanoporous carbon by thermal treatment of ZIF-67, hybridized with  $\text{MnO}_2$ , and demonstrated ORR experiments for fuel cell applications [12]. Amorphous intermediate and crystalline  $\text{Co}_3\text{O}_4$  was synthesized by thermal treatment of ZIF-67 [13], and the amorphous sample showed an OER onset potential of 1.4 V (vs. reference hydrogen electrode, RHE), lower than that (1.52 V) of a crystalline sample. For MXene-supported CoNi-ZIF-67 catalysts by the coprecipitation method, the OER test showed an onset overpotential of 275 mV (vs. RHE) and a Tafel slope of 65.1 mV/dec [15]. B- $\text{Co}_3\text{O}_4$ @ZIF-67 nanocages were synthesized by the hydrothermal method using a sacrificial template, and showed an overpotential of 334 mV at a current density of 10  $\text{mA cm}^{-2}$  and a Tafel slope of 73.88 mV for OER [18]. Another work introduced bimetallic ZIF-8 and ZIF-67 to synthesize Ru-decorated Co/N-codoped porous carbon catalysts, and the HER performance showed an overpotential of 30 mV at 10  $\text{mA cm}^{-2}$  and a Tafel slope of 32.1 mV/dec. The stability was claimed to be superior than a commercial 20 wt% Pt/C [20]. A MOF-derivatized Z-scheme catalyst of  $\text{Fe}_2\text{O}_3$ @Ag-ZnO@C was also introduced to photodegrade tetracyclin and methylene blue in wastewater [21]. The developed catalyst showed high light absorption and charge transfer efficiency for higher photocatalytic performance. For an application area of  $\text{CO}_2$  reduction [25–27], CdS/ZIF-67 nanocomposites were synthesized by a simple wet reaction method and tested for photocatalytic  $\text{CO}_2$  reduction reaction under a 300 W Xe lamp (with 420 nm cut-off filter) [23]. The catalysts showed CO and  $\text{H}_2$  as the main products, with 184  $\mu\text{mol g}^{-1}\cdot\text{h}^{-1}$  and 1098  $\mu\text{mol g}^{-1}\cdot\text{h}^{-1}$ , respectively, and a CO selectivity of 5–45%.

As discussed in the literature, many strategies have been employed and the consequent materials have been tested in various application areas [1–27]. Motivated by this, we seek to further widen the synthesis of ZIP-derivatized catalyst materials and examine new physicochemical properties of a newly synthesized material. Thus, we prepared bean sprout-like Co-TiO<sub>2</sub>/Ti nanostructures by the thermal treatment of ZIF-67/Ti hybrid structure and demonstrated diverse catalytic applications of photocatalytic  $\text{CO}_2$  reduction, electrochemical  $\text{CO}_2$  reduction and electrochemical oxygen evolution reaction. Although ZIF-derivatized catalyst have been extensively studied for water splitting, few studies have been reported related to  $\text{CO}_2$  reduction [25–27]. Therefore, the present study shows some data sets for catalytic performances on  $\text{CO}_2$  reduction. ZIP-67 was chosen because Co is in the structure, and consequent Co oxide-based catalysts have potentially high applicability to water splitting reactions [28]. Cu and Ti were chosen because they have been extensively used as substituent materials and catalyst supports in photocatalysis and electrocatalysis [28–32]. Therefore, the present results provide a useful strategy for the design of new catalyst materials with high efficiency for energy and environment fields via  $\text{CO}_2$  reduction and water splitting.

## 2. Materials and Methods

### 2.1. Preparation of ZIF-67/Ti and Co-TiO<sub>2</sub>/Ti Catalysts

Chemicals were  $\text{Co}(\text{NO}_3)_2\cdot 6\text{H}_2\text{O}$  (97.0%, Samchun Pure Chem., Kyoungki, Korea), 2-methylimidazole (99%, Sigma-Aldrich, Saint Louis, MO, USA) and methanol (MeOH, 99.9%, Samchun Pure Chem., Kyoungki, Korea). For the preparation of ZIF-67/Ti, a Ti sheet was roughened by sandpaper followed by sonication in deionized water for 30 min, and then dipped in 1%  $\text{HNO}_3$  solution for 1 min. After that, the sheet was finally washed with deionized water and dried under an infrared (IR) lamp. For the preparation of ZIF-67/Ti, a solution of  $\text{Co}(\text{NO}_3)_2\cdot 6\text{H}_2\text{O}$  (2mmol) in 40 mL MeOH and a solution of 2-methylimidazole (20 mmol) in 40 mL MeOH were fully mixed, and then the cleaned Ti sheet was dipped in the mixed solution for 16 h to load ZIF-67. The consequent ZIF-67/Ti was then gently washed with MeOH and dried under an IR lamp. After that, the as-prepared ZIF-67/Ti sheet was placed in a tube furnace with Ar gas (99.999%) flow (80 mL/min). The furnace temperature was then increased to 800 °C with a ramp rate of 23 °C/min, and once the temperature reached 800 °C, the power was turned off, and we let the furnace naturally cool to room temperature. Finally, we obtained Co-TiO<sub>2</sub>/Ti nanostructures. Cu deposition

on the nanostructures was performed using a SPT-20 ion sputter coater (COXEM Co., Daejeon, Korea) at an ionization current of 3 mA for 10 s, 30 s, 60 s, 120 s, 240 s, 480 s and 960 s, respectively.

## 2.2. Characterisation of the Catalyst Samples

The crystal phases of the materials formed on Ti sheets were examined using a Mini-Flex II X-ray diffractometer (Rigaku Corp., Tokyo, Japan) with a Cu K $\alpha$  radiation source (CNU Chemistry Core Facility). A VESTA software (ver. 3.5.7, free downloaded at <https://jp-minerals.org/vesta/en/download.html>, accessed on 30 April 2021) was employed for crystal structure building and facet visualization [33]. A FEI Tecnai G2 F30 S-TWIN TEM (FEI-Philips, Hillsboro, OR, USA) at 300 kV was used to obtain high resolution transmission electron microscope (HR-TEM) images. The morphologies of the samples were all examined using a S-4800 (Hitachi Ltd., Tokyo, Japan) scanning electron microscope (SEM) at an acceleration voltage of 10.0 keV. Energy-dispersive X-ray spectroscopy (EDXS) was employed to examine elemental compositions and mapping images using a SEM (Merlin Compact, Carl Zeiss, Germany), coupled with an AZtec Energy X-MaxN EDXS (OXFORD, Oxford, UK). A LabRAM HR-800 UV-Visible-NIR Raman spectrometer (Horiba Jobin Yvon Kyoto, Japan) was used to take Raman spectra with a laser wavelength of 514 nm and a 100 $\times$  objective, and the monochromator grating of 1800. X-ray photoelectron spectra (XPS) were obtained using a K-alpha<sup>+</sup> XPS spectrometer (Thermo-VG Scientific, Waltham, MA, USA) with a hemispherical energy analyzer and a monochromated Al K $\alpha$  X-ray ( $E = 1486.6$  eV) source. Temperature-programmed reaction spectrometry was performed using a QGA quadrupole mass gas analyzer (Hiden Analytical Inc., Warrington, United Kingdom). A ZIF-67/Ti (5 mm  $\times$  30 mm) sample was loaded in a U-tube quartz reactor and heated at a temperature heating rate of 20  $^{\circ}$ C/min under N $_2$  gas (99.999%) flow (80 mL/min). The gas products with temperature were real-time monitored using the QGA analyzer.

## 2.3. Photocatalytic and Electrocatalytic CO $_2$ Reduction Experiments

Photocatalytic CO $_2$  reduction tests were performed in a closed stainless-steel chamber (volume  $\sim$ 40 mL) with a quartz window. A bare (or Cu-deposited) Co-TiO $_2$ /Ti disc (a diameter of 47 mm) was placed inside the chamber. Before being closed, the chamber was flushed and filled with pure CO $_2$  gas (99.999%) with 60  $\mu$ L deionized water inside the chamber. For CO $_2$  reduction test, the sample was placed under UVC light (200–280 nm, a power density of 5.94 mW/cm $^2$ ) through the window for 6 h.

For electrochemical CO $_2$  reduction experiment, a three-electrode connection system was used with a Pt counter electrode, a Ag/AgCl (3.0 M KCl) reference electrode and a Co-TiO $_2$ /Ti electrode (5 mm  $\times$  30 mm) working electrode. The electrochemical workstation was a WPG100 Potentiostat/Galvanostat (WonATech Co., Ltd., Seoul, Korea). We used an air-tight closed glass cell (100 mL) with 50 mL 0.1 M NaHCO $_3$  electrolyte. Amperometry was performed at a potential of  $-1.8$  V (vs. Ag/AgCl) for 3 h.

After the amperometry (or the photocatalytic reaction under UVC condition for 6 h), 0.5 mL volume of gas from the air-tight closed electrochemical cell (or the closed stainless-steel chamber) was taken and injected into a YL 6500 gas chromatography (GC) system (Young In Chromass Co., Ltd., Seoul, Korea) for the analysis of CO $_2$  reduction gas products. The GC system was equipped with a Ni catalyst methanizer assembly, a thermal conductivity detector (TCD), a flame ionization detector (FID), two different columns of 40/60 Carboxen-1000 (Sigma-Aldrich, St. Louis, MO, USA) and HP-PlotQ-PT (Agilent Technologies, Inc., Santa Clara, CA, USA).

Electrochemical oxygen evolution reaction (OER) tests were also performed using a three-electrode system (a Pt counter electrode, a Hg/HgO reference electrode and a Co-TiO $_2$ /Ti electrode working electrode). The electrochemical workstation was a WizECM-1200 Premium potentiostat/galvanostat (WizMAC, Daejeon, Korea). Linear sweep voltam-

metry (LSV) was carried out at a scan rate of 20 mV/s in 0.1 M KOH electrolyte (a volume of 50 mL), with a potential range from  $-0.05$  V to  $+1.5$  V.

### 3. Results and Discussion

Figure 1a shows the sample preparation method and photos of the samples at each stage. The polished Ti sheet appeared bright gray and became violet upon loading ZIF-67. Upon thermal treatment at  $800$  °C, the color finally became uniform blue-gray. This indicates that surface morphology and crystal phase became changed after the thermal treatment. Figure 1b displays temperature-programmed reaction (TPR) profiles for the as-prepared ZIF-67 on Ti sheet to examine thermal decomposition of the ZIF-67 on the Ti surface. It was observed that TPR signal of  $\text{CO}_2$  (mass = 44 amu) started to increase at around  $350$  °C, maximize at  $490$  °C and return to the background signal above  $510$  °C. This indicates that ZIF-67 decomposed at around  $490$  °C. This result is consistent with the literature [34].

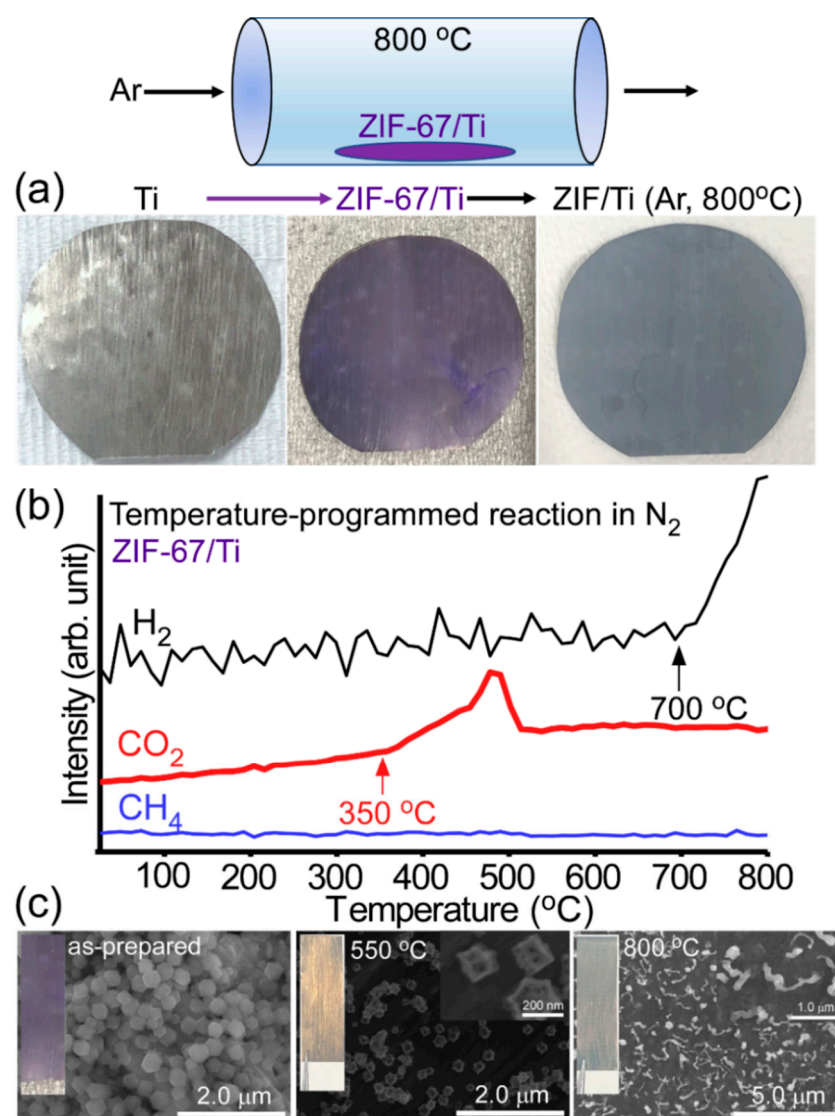


**Figure 1.** Schematic of a reaction setup and photos of the samples at each stage (a); temperature-programmed reaction profiles (b) of  $\text{H}_2$ ,  $\text{CO}_2$  and  $\text{CH}_4$  for ZIF-67/Ti sheet; and SEM images (c) of as-prepared ZIF-67/Ti and after thermal treatments of  $550$  °C and  $800$  °C, respectively.

The TPR signal (Figure 1b) of  $\text{H}_2$  (mass = 2 amu) started to increase at  $700$  °C, which was attributed to the association of adsorbed H, followed by  $\text{H}_2$  release. The  $\text{CH}_4$  signal

showed no critical change. The corresponding SEM images (Figure 1c) at each stage (as-prepared, 550 °C and 800 °C conditions) clearly showed different morphologies. For the SEM image of the as-prepared ZIF-67/Ti, the morphology appeared to be polyhedron shape with sizes of 30–40 nm. This is consistent with the literature regarding ZIF-67 [15]. After thermal treatment up to 550 °C, ZIF-67 became shrunken and hollow, which was attributed to the thermal decomposition at 490 °C, as discussed above. Interestingly, the morphology drastically changed after thermal treatment up to 800 °C. The corresponding SEM image appeared as bean sprouts with head and stem. The head appeared to be grown from the surface of Ti surface. This is further discussed below.

Three samples of ZIF-67/Ti, Co-TiO<sub>2</sub>/Ti, Cu(960 s)-Co-TiO<sub>2</sub>/Ti were selected, and their XRD profiles were obtained and displayed in Figure 2. For the XRD patterns of a ZIF-67 loaded Ti sheet, several major peaks were observed at  $2\theta = 35.2^\circ, 38.5^\circ, 40.2^\circ, 53.1^\circ, 63.1^\circ$  and  $70.8^\circ$ , assigned to the (010), (002), (011), (012), (110) and (013) planes of hexagonal metallic Ti (ICSD ref. # 98-004-3614), respectively. These peaks were commonly observed for all the samples attributed to metallic Ti support. A sharp peak around  $2\theta = 8.5^\circ$  was attributed to the crystal phase of ZIF-67 [13–15]. For the XRD patterns of Co-TiO<sub>2</sub>/Ti sample, several peaks newly appeared at  $2\theta = 27.4^\circ, 36.0^\circ, 39.1^\circ, 41.2^\circ, 44.0^\circ, 54.2^\circ, 56.5^\circ$  and  $63.9^\circ$ , and were assigned to the (110), (011), (020), (111), (120), (121), (220) and (130) crystal planes of tetragonal rutile TiO<sub>2</sub> (ICSD ref. # 98-003-3838), respectively. Other strong peaks were observed at  $2\theta = 29.1^\circ, 39.8^\circ, 52.3^\circ$  and  $69.5^\circ$ , and matched the crystal planes of (006), (11-3), (116) and (11-9) for hexagonal Ti<sub>3</sub>O (ICSD ref. # 98-003-6055), respectively. The expanded XRD profiles between  $2\theta = 34^\circ$  and  $45^\circ$  clearly show that metallic Ti and hexagonal Ti<sub>3</sub>O coexist in the thermal (800 °C)-treated samples [35]. The XRD patterns of Co and Cu oxides were hardly seen in the XRD profiles. This is further discussed below.

Figure 3 shows the SEM images of the as-prepared ZIF-67/Ti (Figure 3a) and Co-TiO<sub>2</sub>/Ti (Figure 3(b,b1)) and Cu (960 s)-Co-TiO<sub>2</sub>/Ti (Figure 3(c,c1)) samples. As discussed above, the polyhedron shape in Figure 3a was due to ZIF-67, and was commonly reported in the literature [15]. For the SEM image of Co-TiO<sub>2</sub>/Ti, the morphology appeared to be bean sprouts with head and stem. For Cu (960 s)-Co-TiO<sub>2</sub>/Ti (Figure 3(c,c1)) samples, the head and the stem appeared to be fully covered by Cu. For the TEM images of the bean sprout nanostructures in Figure 3d,e, two regions (f = head and g = stem) were selected to obtain HRTEM images. For the HRTEM image of the head (Figure 3f), clear lattice fringes were seen with a distance of 0.277 nm. This is in good agreement with the lattice spacing of the (220) plane of cubic phase Co<sub>3</sub>O<sub>4</sub> [36]. The corresponding fast-Fourier-transform (FFT) pattern (Figure 3(f1)) shows high crystallinity of the head. For the HRTEM image of the stem (Figure 3g), a clear lattice spacing of 0.322 nm was observed, and the corresponding FFT pattern (Figure 3(g1)) showed high single crystalline nature of the stem. The lattice spacing was consistent with the (110) plane of tetragonal rutile TiO<sub>2</sub> [37], which was observed by the XRD, discussed above. For visual understating of the crystal phase and the facet, the crystal structure projections with the crystal planes are displayed in Figure 3(f2,g2) for Co<sub>3</sub>O<sub>4</sub> and TiO<sub>2</sub>, respectively.

Figure 4 shows layered and single elemental (Co, Ti, O, and Cu) EDXS mapping images and EDXS profiles of Co-TiO<sub>2</sub>/Ti and Cu (960 s)-Co-TiO<sub>2</sub>/Ti samples. As discussed above in the above SEM images (Figure 3(b,b1,c,c1)) and the SEM images in Figure 4(a1,b1), Co-TiO<sub>2</sub>/Ti nanostructures appeared to be bean sprouts with head and stem. To confirm the chemical elements of the head and stem, elemental EDXS mapping images were obtained. On the basis of the images, Co EDXS signal was mainly localized on the head, indicating that the head was mainly due to Co elements while others were mainly due to Ti oxides. This is in good agreement with the TEM/HRTEM results discussed above. The Co and Ti oxide were originated from the ZIF-67 and Ti support, respectively. Upon Cu-deposition, Cu EDXS signal was newly detected. The EDXS profiles (Figure 4(a2,b2)) clearly confirmed the elements of Ti, Co, surface C and Cu (after Cu-deposition), Ti (0.395, 0.452, 4.511, and 4.932 keV), O (0.525 keV), C (0.277 keV), Co (0.678, 0.694, 0.776, 6.93 and 7.65 keV) and Cu (0.811, 0.832, 0.93, 8.048 and 8.905 keV) [38]. For the Co-TiO<sub>2</sub>/Ti sample, the atomic % ratios

of C, Ti O, and Co were estimated to be 3.7%, 28.9%, 64.8% and 2.6%, respectively. The Co/Ti ratio (%) was estimated to be  $2.6\%/28.9\% = 9.0/100$ . For the Cu (960 s)-Co-TiO<sub>2</sub>/Ti sample, the atomic % ratios of C, Ti, O, Co and Cu were estimated to be 2.6%, 35.2%, 58.6%, 2.5% and 1.0%, respectively. The Co/Ti ratio (%) was estimated to be  $2.5\%/35.2\% = 7.1/100$ .

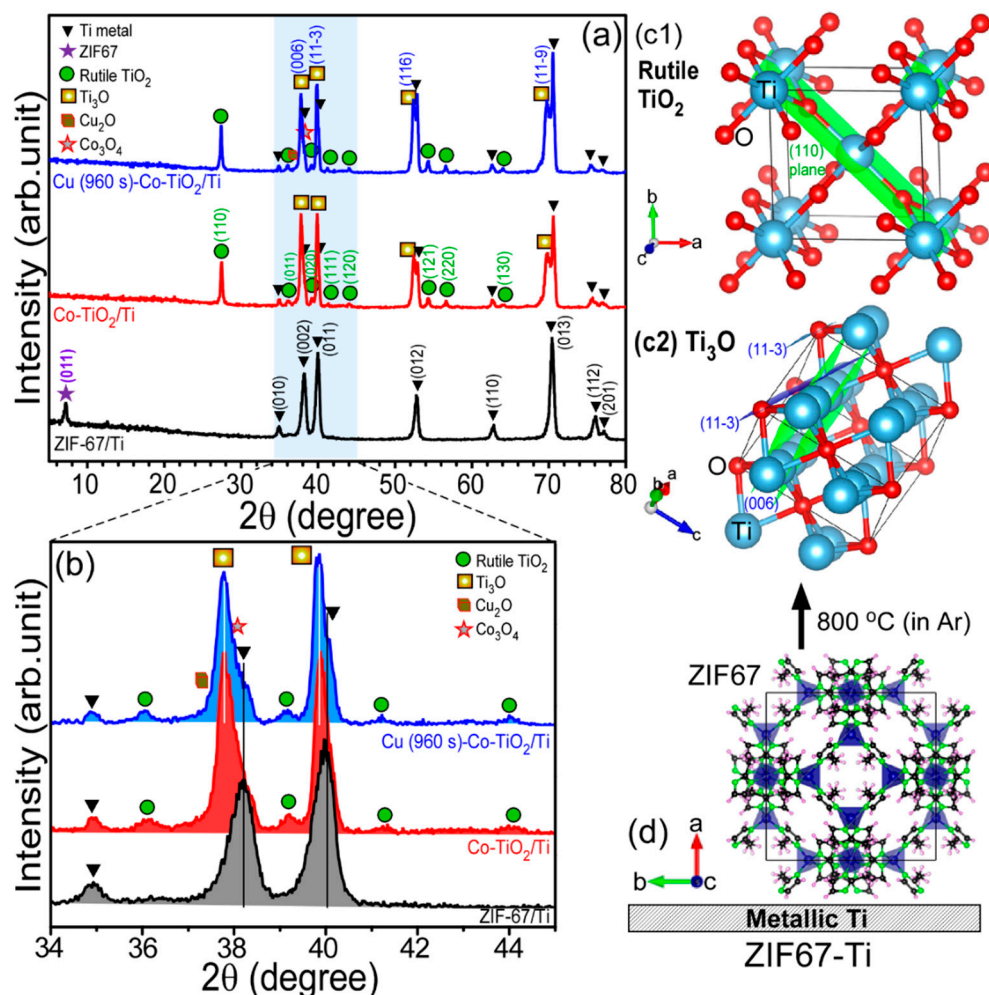


**Figure 2.** XRD diffraction patterns (a) of as-prepared ZIF-67/Ti, Co-TiO<sub>2</sub>/Ti, Cu (960 s)-Co-TiO<sub>2</sub>/Ti samples; expanded XRD regions (34–45°) (b); crystal structure projections of rutile TiO<sub>2</sub> (c1); and Ti<sub>3</sub>O (c2); and a cartoon of ZIF67 loaded on Ti support (d).

Figure 5 displays the Raman spectra for ZIF-67/Ti, Co-TiO<sub>2</sub>/Ti, Cu (60 s)-Co-TiO<sub>2</sub>/Ti and Cu (960 s)-Co-TiO<sub>2</sub>/Ti samples. For the spectrum of ZIF-67/Ti, several sharp peaks were observed at 125 cm<sup>-1</sup>, 173 cm<sup>-1</sup>, 209 cm<sup>-1</sup>, 251 cm<sup>-1</sup>, 312 cm<sup>-1</sup>, 423 cm<sup>-1</sup> and 683 cm<sup>-1</sup>. These peaks are attributed to ZIF-67 commonly reported in the literature [39]. For the Raman spectrum of a Co-TiO<sub>2</sub>/Ti sample, very broad and strong Raman peaks were observed at 270 cm<sup>-1</sup>, 439 cm<sup>-1</sup> and 610 cm<sup>-1</sup>, in addition to weaker and sharper Raman peaks at 141 cm<sup>-1</sup>, 192 cm<sup>-1</sup>, 482 cm<sup>-1</sup>, 522 cm<sup>-1</sup>, 620 cm<sup>-1</sup> and 689 cm<sup>-1</sup>. Three characteristic Raman active peaks at 141 cm<sup>-1</sup>, 439 cm<sup>-1</sup> and 610 cm<sup>-1</sup> could be assigned to the B<sub>1g</sub>, E<sub>g</sub> and A<sub>1g</sub> modes of rutile TiO<sub>2</sub>, respectively [40,41]. The corresponding peak at 240 cm<sup>-1</sup> is due to the multi-phonon scattering process [41]. In addition to the Raman peaks of TiO<sub>2</sub>, five other Raman active peaks were observed at 192 cm<sup>-1</sup>, 482 cm<sup>-1</sup>, 522 cm<sup>-1</sup>, 620 cm<sup>-1</sup> and 689 cm<sup>-1</sup>, assigned to F<sub>2g</sub>, E<sub>g</sub>, F<sub>2g</sub>, F<sub>2g</sub> and A<sub>1g</sub> modes of Co<sub>3</sub>O<sub>4</sub>, respectively [42,43]. On the basis of the results, it was concluded that the major was TiO<sub>2</sub> (the stem) and minor was Co<sub>3</sub>O<sub>4</sub> (the head) in the bean sprout nanostructures.

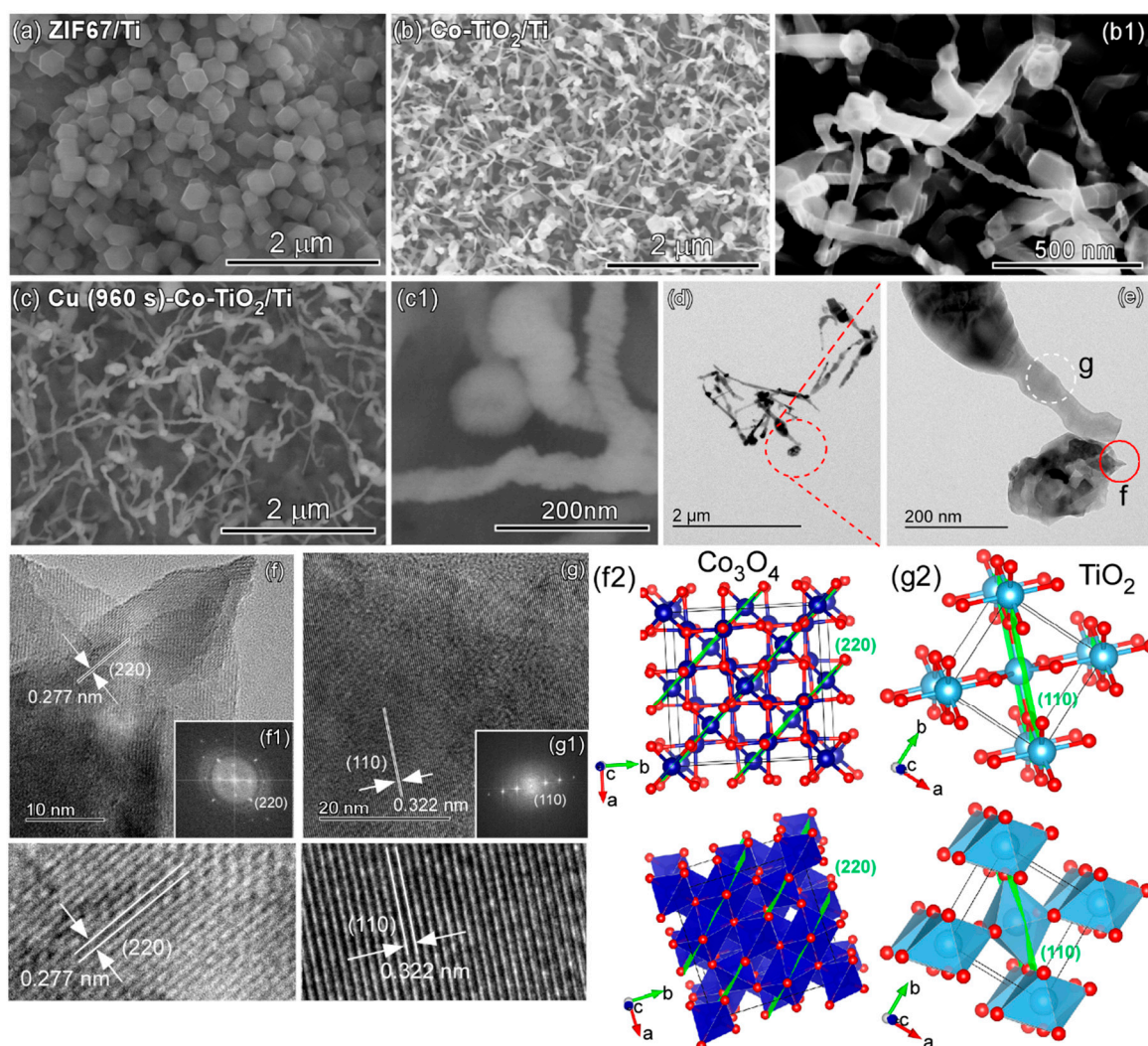


**Figure 3.** SEM images of ZIF67-Ti (a), Co-TiO<sub>2</sub>/Ti (b,b1), Cu (960 s)-Co-TiO<sub>2</sub>/Ti (c,c1). TEM (d,e) and HRTEM (f,g) images of Co-TiO<sub>2</sub>/Ti. Insets show the corresponding FFT patterns (f1,g1) and the structure projection (f2,g2) of the (220) and (110) planes for Co<sub>3</sub>O<sub>4</sub> (f2) and rutile TiO<sub>2</sub> (g2), respectively.

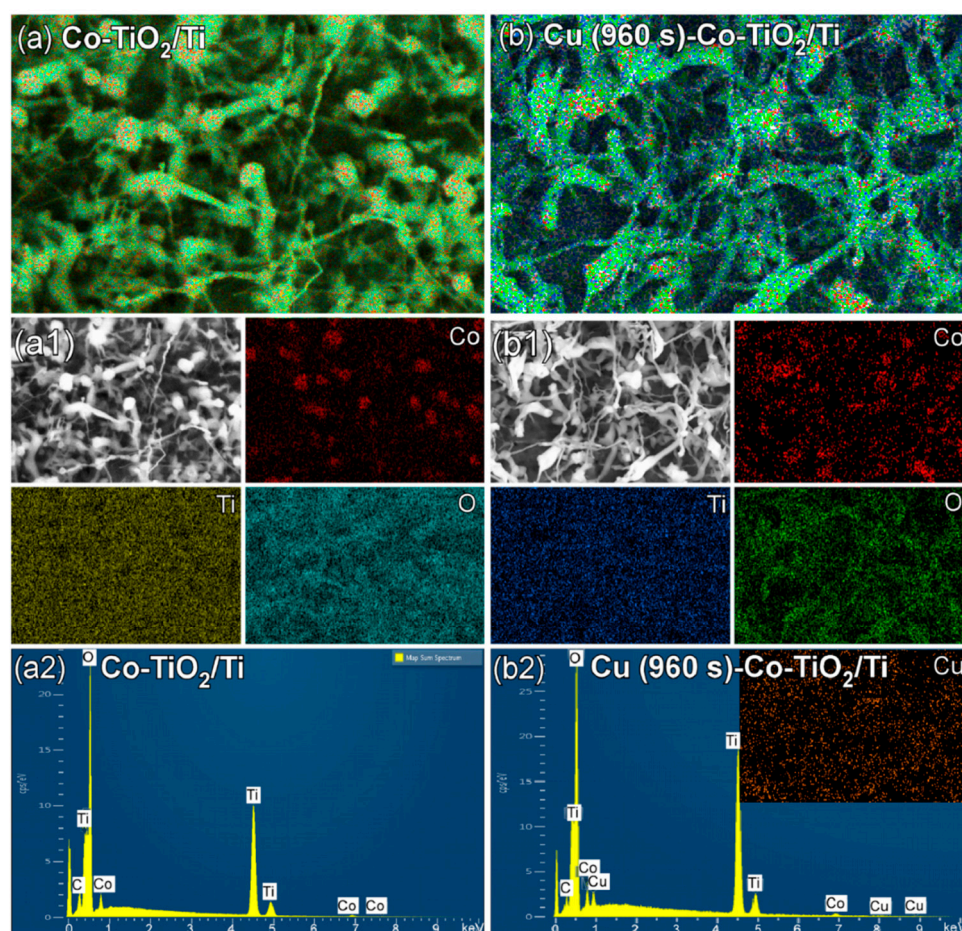
Upon Cu deposition for 60 s, no characteristic of Cu species was observed. However, interestingly, the A<sub>1g</sub> mode at 689 cm<sup>-1</sup> was substantially increased relative to the other Raman peaks. Furthermore, in the normalized Raman peaks of ZIF-67/Ti (red line) and Cu (960 s)-Co-TiO<sub>2</sub>/Ti (green line) samples (Figure 5b), the A<sub>1g</sub> mode became substantially enhanced after Cu deposition for 960 s. The Raman peaks for the Cu species were not clearly detected [44,45]. As depicted in Figure 5c, it may appear that Ti<sub>3</sub>O was formed at the interface of Ti and TiO<sub>2</sub>, and Co<sub>3</sub>O<sub>4</sub> was grown as a head during thermal deposition of ZIF-67, as discussed in Figure 1b above.

Figure 6 displays Ti 2p (Figure 6a), Co 2p (Figure 6b), Cu 2p (Figure 6c) and O 1s (Figure 6d) XPS profiles for bare Co-TiO<sub>2</sub>/Ti and Cu deposited (10 s, 60 s and 240 s) Co-TiO<sub>2</sub>/Ti samples before and after UVC photocatalytic CO<sub>2</sub> reduction tests. The elements of Ti, Co, C and O were commonly observed as expected, and the Cu element was additionally observed after Cu deposition. On the basis of the Ti 2p and Co 2p XPS intensities and sensitivity factors, the Co/Ti XPS ratio was estimated to be 5.3/100 for bare Co-TiO<sub>2</sub>/Ti. The Co/Ti XPS ratio became 3.7/100 after Cu deposition for 240 s. As discussed above, the decrease in Co/Ti was also observed in the EDXS data, which is consistent with the XPS data. This indicates that the head of Co is covered more by Cu compared to the stem of Ti.

For the Ti 2p XPS profiles of bare Co-TiO<sub>2</sub>/Ti (Figure 6a), the Ti 2p<sub>3/2</sub> and Ti 2p<sub>1/2</sub> peaks were observed at binding energies (BEs) of 457.7 eV and 463.4 eV, respectively, with

a spin-orbit (S-O) splitting energy of 5.7 eV. These peaks were attributed to Ti(IV) state of  $\text{TiO}_2$  [30]. The Ti 2p BE peaks showed no critical change with an increasing Cu deposition time, but the intensity was somewhat decreased due to overlayer Ti. Furthermore, the asymmetry of the Ti 2p peak was increased with an increasing Cu deposition (Supplemental Information, Figure S1a). The Ti 2p XPS signal appeared to increase around 459 eV and 465 eV. The asymmetry of Ti 2p XPS peak could be a change in either chemical state or physical nature [46].

In Figure 6b, the corresponding Co 2p<sub>3/2</sub> and Co 2p<sub>1/2</sub> peaks were observed at 779.3 eV and 794.7 eV, respectively, with an S-O splitting energy of 15.4 eV. These peaks could be assigned to  $\text{Co}_3\text{O}_4$ , as expected from the HRTEM and Raman spectra. The Co 2p peak showed no substantial change with increasing Cu deposition time based on the normalized Co 2p XPS spectra with Cu deposition time (Supplemental Information, Figure S1b), but the intensity decreased because of the overlayer Cu.



**Figure 4.** Layered (a,b) and elemental (Co, Ti, O and Cu (a1,b1)) mapping images and EDXS profiles (a2,b2) of  $\text{Co-TiO}_2/\text{Ti}$  (a,a1,a2) and  $\text{Cu (960 s)-Co-TiO}_2/\text{Ti}$  (b,b1,b2).

The corresponding O 1s XPS peaks (Figure 6d) showed two broad peaks 528.8 eV and 530.7 eV, attributed to lattice oxygen ( $\text{O}_{\text{lattice}}$ ) of metal oxide and surface oxygen species (e.g.,  $\text{O}_{\text{ad}}$ : OH/ $\text{H}_2\text{O}$  and defects), respectively [30]. With increasing Cu deposition time, the higher BE peak at 530.7 eV was observed to be enhanced (Supplemental Information, Figure S1c), which was attributed to increase in surface oxygen species. For the bare  $\text{Co-TiO}_2/\text{Ti}$  sample, the XPS  $\text{O}_{\text{ad}}/\text{O}_{\text{lattice}}$  ratio was measured to be 17.4%/82.6% and the ratios became 16.0%/84.0%, 24.7%/75.2% and 50.5%/49.5% after Cu deposition for 10 s, 60 s and 240 s, respectively.



For the Cu 2p XPS profile of Cu-deposited (10 s and 60 s) Co-TiO<sub>2</sub>/Ti samples (Figure 6c), the Cu 2p<sub>3/2</sub> and Cu 2p<sub>1/2</sub> peaks were commonly observed at 932.0 eV and 951.5 eV, respectively, with an S-O splitting energy of 19.5 eV. These peaks could be assigned to Cu<sub>2</sub>O and/or metallic Cu [46–48]. For the bare Co-TiO<sub>2</sub>/Ti sample, no Cu XPS signal was observed, as expected. For the Cu 2p XPS profile of Co-TiO<sub>2</sub>/Ti sample after Cu-deposition for 240 s, additional Cu 2p<sub>3/2</sub> and Cu 2p<sub>1/2</sub> peaks were observed at 933.7 eV and 952.8 eV, respectively, with an S-O splitting energy of 19.1 eV. Moreover, broad shake-up structures (☆) were newly observed around 942 eV and 962 eV. These new Cu 2p peaks and the characteristic shake-up features have commonly been attributed to CuO (cupric oxide) [46–48].

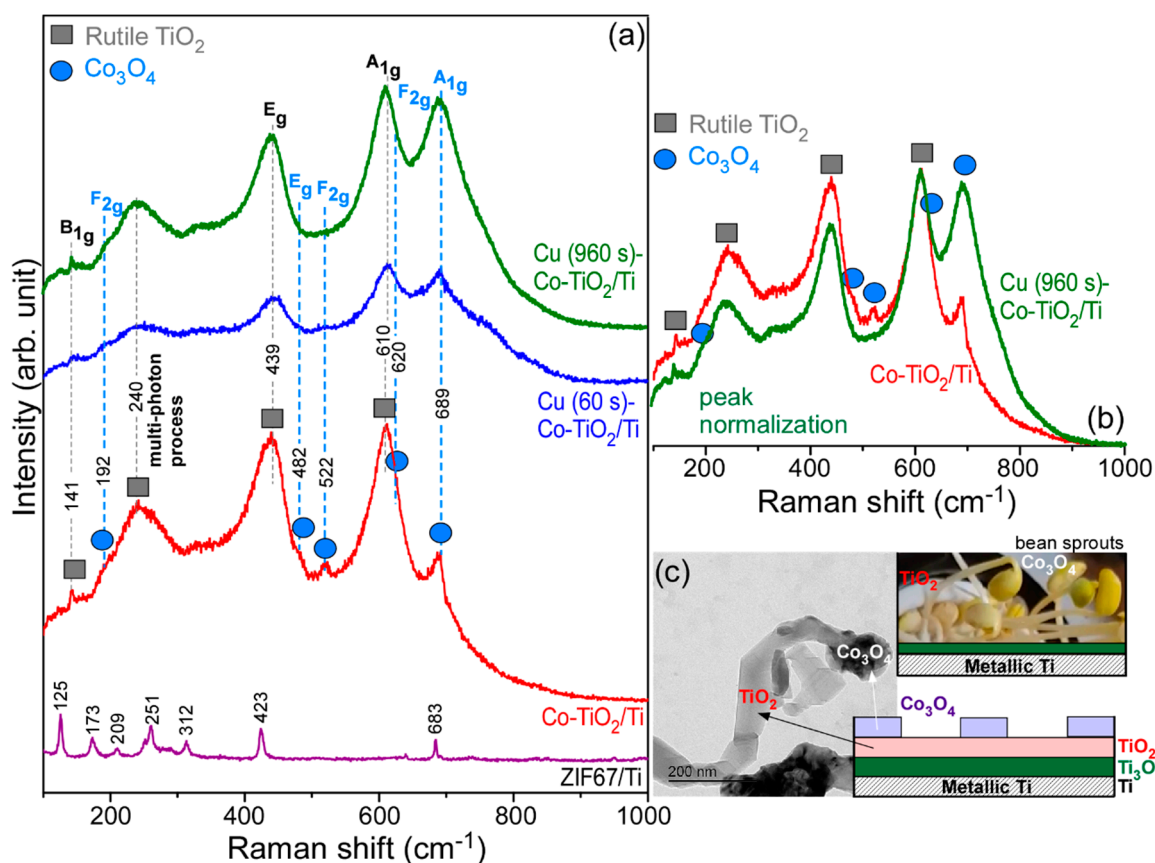


**Figure 5.** Raman spectra (a) of ZIF-67/Ti, Co-TiO<sub>2</sub>/Ti, Cu (60 s)-Co-TiO<sub>2</sub>/Ti and Cu (960 s)-Co-TiO<sub>2</sub>/Ti corresponding to normalized Raman spectra (b) before and after Cu deposition, and a schematic (c) of the material growth mode on metallic Ti surface upon thermal treatment.

For the XPS profiles after photocatalytic CO<sub>2</sub> reduction tests, Ti 2p peaks of bare and Cu (10 s)-Co-TiO<sub>2</sub>/Ti samples were decreased, while the Co 2p signal was relatively increased. At higher Cu coverages of 60 s and 240 s, Ti 2p signal was enhanced, as was the Co 2p signal. The normalized Ti 2p peaks showed no critical difference with Cu thickness after CO<sub>2</sub> reduction (Supplemental Information, Figure S1(a1–a3)). However, for the Co 2p XPS of Cu (240 s)-Co-TiO<sub>2</sub>/Ti sample (Figure 6b), satellite peaks at 786 eV and 802 eV were enhanced after the photocatalytic CO<sub>2</sub> reduction, which was attributed to an increase in CoO state (Supplemental Information, Figure S1(b1–b3)) [15,27,43,48]. For the O 1s XPS profiles, the XPS O<sub>ad</sub>/O<sub>lattice</sub> ratios were substantially changed after the photocatalytic CO<sub>2</sub> reduction. The O<sub>ad</sub>/O<sub>lattice</sub> ratios were 51.9%/48.1%, 49.2%/50.8%, 19.6%/80.4% and 53.9%/46.1% for bare, Cu(10 s)-, Cu (60 s)- and Cu (240 s)-Co-TiO<sub>2</sub>/Ti samples, respectively. Except for the Cu (60 s)-Co-TiO<sub>2</sub>/Ti sample, the O<sub>ad</sub> XPS peak was significantly enhanced after the photocatalytic CO<sub>2</sub> reduction (Supplemental Information, Figure S1(c1)). For the

Cu 2p XPS profile of the Cu (240 s)-Co-TiO<sub>2</sub>/Ti sample after the reduction test, the intensity was somewhat decreased (Supplemental Information, Figure S1d), which was possibly due to agglomeration of smaller Cu particles forming larger Cu particles. In addition, the Cu 2p<sub>3/2</sub> (Cu 2p<sub>1/2</sub>) peak at 933.7 eV (952.8 eV) became stronger than the peaks at 932.0 eV (951.5 eV). This is mainly due to CuO species being more present than Cu<sub>2</sub>O species. Carbon signals were somewhat increased both at 284 eV and 288 eV after photocatalytic CO<sub>2</sub> reduction (Supplemental Information, Figure S1e), which was attributed to an increase in C–C and C=O species.

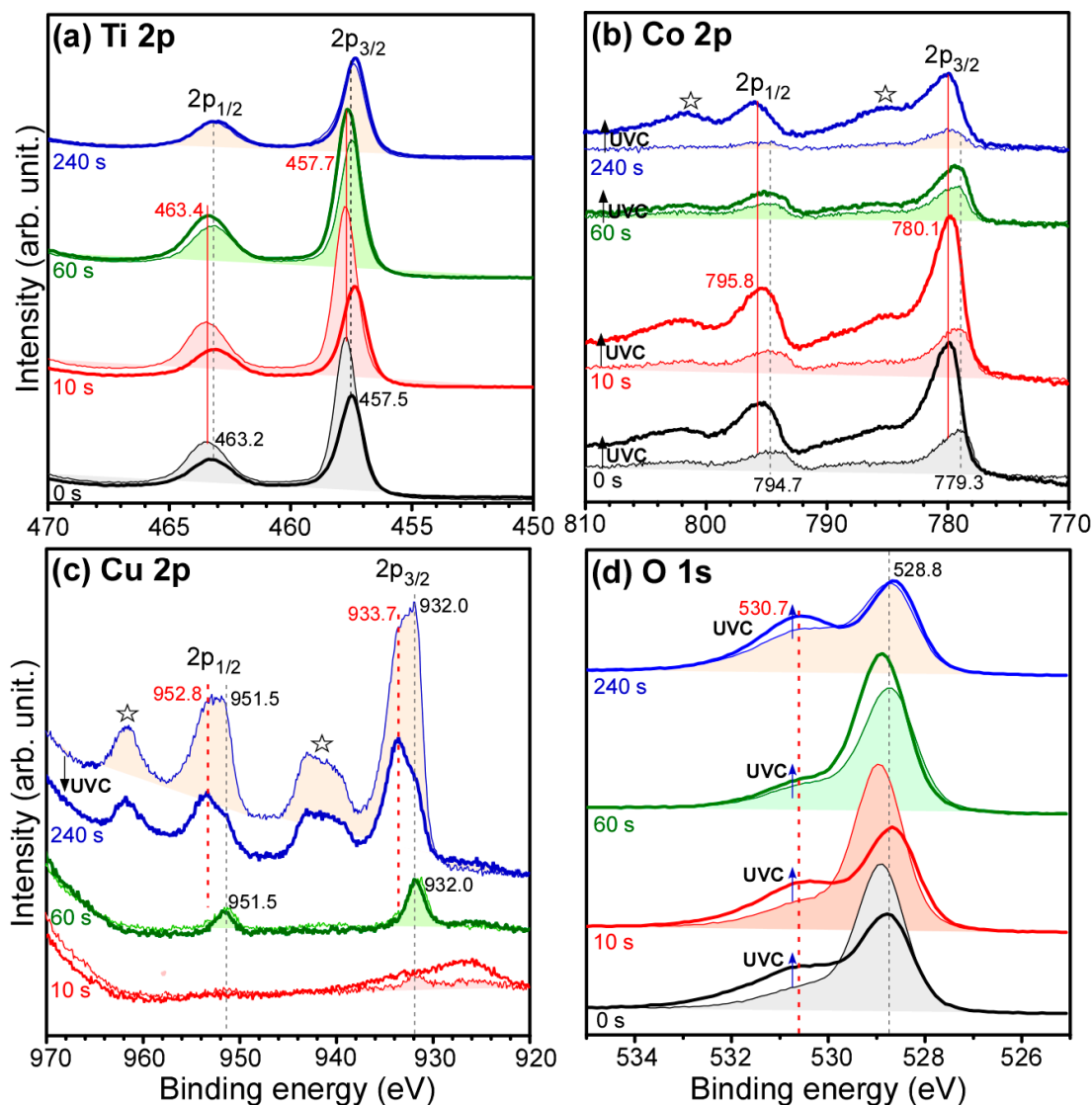


**Figure 6.** Ti 2p (a), Co 2p (b), Cu 2p (c) and O 1s (d) XPS profiles for bare Co-TiO<sub>2</sub>/Ti and 10s, 60 s and 240 s-Cu-deposited Co-TiO<sub>2</sub>/Ti samples before (thin lines) and after (thick lines) UVC photocatalytic reaction. ☆ I indicates shake-up structures.

Photocatalytic CO<sub>2</sub> reduction experiments [30,48–52] were performed, and the amounts in the reduction products are displayed in Figure 7a. The products were commonly observed to be MeOH, CO, CH<sub>4</sub>, C<sub>2</sub>H<sub>2</sub>, C<sub>2</sub>H<sub>4</sub> and C<sub>2</sub>H<sub>6</sub>. The yields (μmol/mol = ppm) of the three major products commonly showed the order of CH<sub>4</sub> < CO < MeOH. For the minor products, C<sub>2</sub>H<sub>2</sub> was also detected in the range of 1.0–4.0 ppm. Although the production amounts were below 1 ppm, C<sub>2</sub>H<sub>4</sub> and C<sub>2</sub>H<sub>6</sub> were meaningfully detected in the gas chromatography (GC) profiles. No H<sub>2</sub> was detected in the GC profile. Choi et al. performed a photocatalytic CO<sub>2</sub> reduction test for a bare Co<sub>3</sub>O<sub>4</sub> powder sample under the same experimental conditions as in the present study, except for a reaction time of 13 h vs.

6 h [52]. They reported that three major products showed the order of  $\text{CH}_4$  (17.1 ppm) < MeOH (19.1 ppm) < CO (83.2 ppm) for 13 h. Lin et al. reported CO as a major photocatalytic  $\text{CO}_2$  reduction product for  $[\text{Co}(\text{bipy})_3]^{2+}$ -embedded  $\text{TiO}_2$  hollow spheres [53]. On the basis of the literature and the present study, MeOH production was highly enhanced in the developed Co- $\text{TiO}_2/\text{Ti}$  nanostructure.

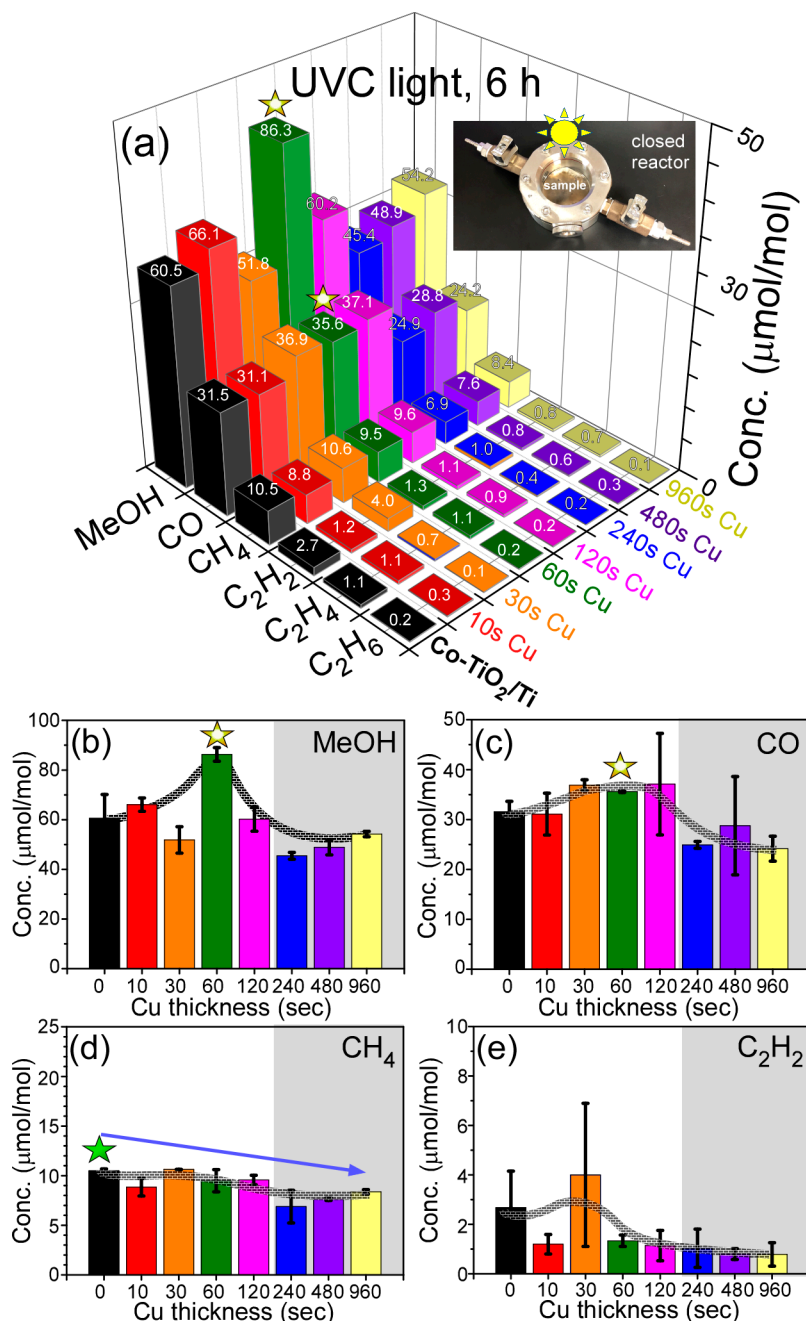


**Figure 7.** Photocatalytic  $\text{CO}_2$  reduction yields: (a) for bare Co- $\text{TiO}_2/\text{Ti}$  and 10s, 60 s, 120 s, 240 s, 480 s and 960 s-Cu-deposited Co- $\text{TiO}_2/\text{Ti}$  samples, and MeOH (b), CO (c),  $\text{CH}_4$  and (d)  $\text{C}_2\text{H}_2$  (e) yields ( $\mu\text{mol/mol}$ ) with error bars. Photo is a closed stainless reactor with a Co- $\text{TiO}_2/\text{Ti}$  disc inside. The asterisk indicates the maximum point.

For the bare Co- $\text{TiO}_2/\text{Ti}$  sample, MeOH, CO,  $\text{CH}_4$ ,  $\text{C}_2\text{H}_2$ ,  $\text{C}_2\text{H}_4$  and  $\text{C}_2\text{H}_6$  were observed to be 60.5 ppm, 31.5 ppm, 10.5 ppm, 2.7 ppm, 1.1 ppm and 0.2 ppm. MeOH production (Figure 7b) showed the highest production of 86.3 ppm after Cu deposition for 60 s. Above Cu deposition of 240 s, MeOH production was observed to be lower than

that in the bare Co-TiO<sub>2</sub>/Ti sample. CO production (Figure 7c) was somewhat increased upon Cu deposition for 30 s–120 s. Upon Cu deposition above 240 s, CO production was also observed to be lower than that in the bare Co-TiO<sub>2</sub>/Ti sample. For CH<sub>4</sub> production (Figure 7d), the bare Co-TiO<sub>2</sub>/Ti sample showed the highest amount of 10.5 ppm, and the yield was gradually decreased with an increasing Cu deposition amount. For C<sub>2</sub>H<sub>2</sub> production (Figure 7e), the amount was higher when Cu amount was below 30 s, but the amount dropped below 1 ppm when Cu deposition was above 60 s. CO<sub>2</sub> reduction selectivities were estimated to be 50–64%, 27–35% and 7–10% for MeOH, CO and CH<sub>4</sub>, respectively. Details are shown in the Supplemental Information, Figure S2. The 60 s-Cu-deposited Co-TiO<sub>2</sub>/Ti sample showed the highest selectivity of 64% for photocatalytic MeOH production.

Conclusively, photocatalytic CO<sub>2</sub> reduction activity became evidently poorer upon Cu deposition above 240 s, which was attributed to less light absorption by thicker Cu film. However, Cu deposition between 30 s and 120 s showed meaningful enhancement in CO<sub>2</sub> reduction activity.

Electrochemical CO<sub>2</sub> reduction experiments [30,49,54,55] were also performed, and the amounts of reduction products are displayed in Figure 8a. In this experimental setup, gaseous products were only measured by GC and no MeOH was detected in the gas phase. The reproducibly detected gaseous products include CO, CH<sub>4</sub>, C<sub>2</sub>H<sub>2</sub>, C<sub>2</sub>H<sub>4</sub> and C<sub>2</sub>H<sub>6</sub>. The amounts were much less than 50 ppm. However, H<sub>2</sub> was significantly detected with the amounts up to 13,325 ppm. Faradaic efficiency (FE, %) for H<sub>2</sub> production was estimated to be about 6–10% in the NaHCO<sub>3</sub> electrolyte condition. CO and CH<sub>4</sub> productions over the bare Co-TiO<sub>2</sub>/Ti sample were observed to be 4.3 ppm and 8.1 ppm, and C<sub>2</sub>H<sub>2</sub>, C<sub>2</sub>H<sub>4</sub> and C<sub>2</sub>H<sub>6</sub> were merely detected with 0.1 ppm–0.5 ppm.

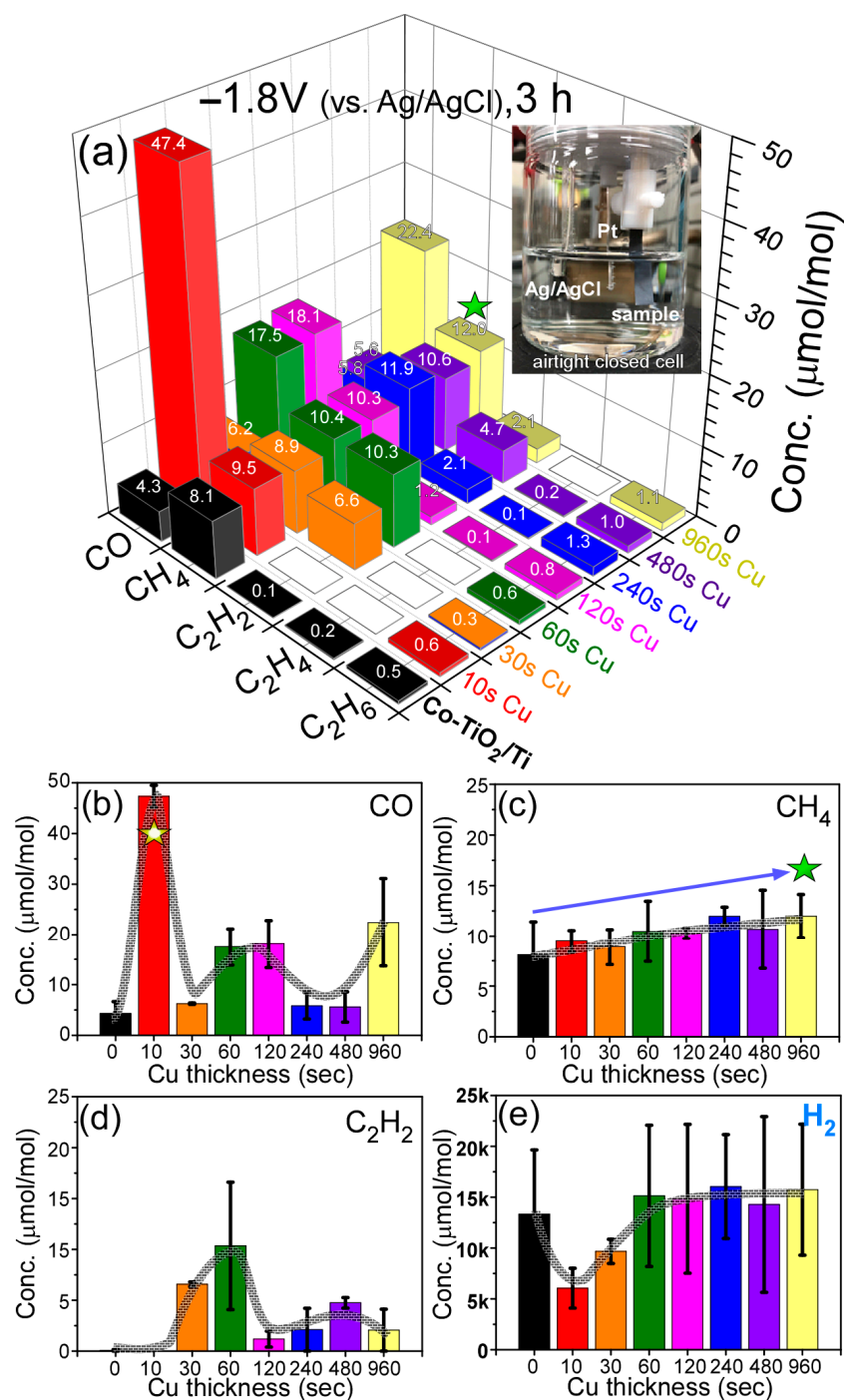


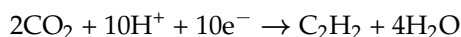
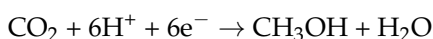
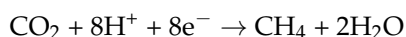
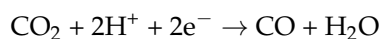
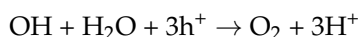
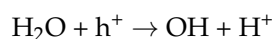
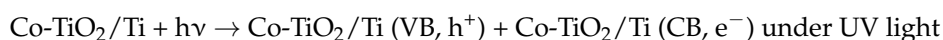
**Figure 8.** Electrochemical CO<sub>2</sub> reduction product yields (a) for bare Co-TiO<sub>2</sub>/Ti and 10s, 30 s, 60 s, 120 s, 240 s, 480 s and 960 s-Cu-deposited Co-TiO<sub>2</sub>/Ti samples, and CO (b), CH<sub>4</sub> (c), C<sub>2</sub>H<sub>2</sub> (d) and H<sub>2</sub> (e) yields (μmol/mol) with error bars. Photo is the electrochemical 3-electrode air-tight closed cell. The asterisk indicates the maximum point for CH<sub>4</sub>.

When Cu was sputter-deposited for 10 s, CO was substantially increased to 47.4 ppm (Figure 8b); this is an 11× increase compared with that in the bare Co-TiO<sub>2</sub>/Ti sample. Upon Cu deposition above 30 s, the CO production was less than that for the Cu (10 s)-Co-TiO<sub>2</sub>/Ti sample, but higher than in the bare Co-TiO<sub>2</sub>/Ti sample. In Figure 8c, the CH<sub>4</sub> production was gradually increased with an increasing Cu deposition, reaching 12.0 ppm upon Cu deposition for 960 s. Inversely, as discussed above (Figure 7d), CH<sub>4</sub> production decreased with increasing Cu deposition in the photocatalytic CO<sub>2</sub> reduction. For C<sub>2</sub>H<sub>2</sub>

production in Figure 8d, the production was  $\leq 0.1$  ppm when the Cu deposition was less than 10 s. However, the amounts were increased and detected with 6.6 ppm and 10.3 ppm upon Cu deposition for 30 s and 60s, respectively. Above 60 s and up to 960 s, the amounts were somewhat decreased and detected with 1.2 ppm–4.7 ppm. The  $C_2H_4$  productions were less than 0.2 ppm for all samples.  $C_2H_6$  was meaningfully detected in the range of 0.5–1.3 ppm and generally increased with increasing Cu amounts.  $H_2$  was more substantially produced, as mentioned above. Above 60 s and up to 960 s,  $H_2$  productions were detected with 14,275 ppm–15,732 ppm with FE (%) of 6.5–7.5%.  $H_2$  production was dominant and all the catalysts showed an  $H_2$  production selectivity of  $>99\%$ . For the  $C_n$  compounds with a total of less than 1% selectivity, the relative selectivities are shown in the Supplemental Information, Figure S3.

We also tested the effect of applied potential for a selected sample of Cu (120 s)-Co-TiO<sub>2</sub>/Ti (Supplemental Information, Figure S4). Interestingly,  $H_2$  production was increased by 4.6× at  $-1.8$  V compared with that at  $-1.5$  V (vs. Hg/HgO). However, CO and  $C_2H_2$  productions were higher at  $-1.5$  V (vs. Hg/HgO). CO was detected with 30.4 ppm and 18.1 ppm at  $-1.5$  V and  $-1.8$  V, respectively.  $C_2H_2$  was detected with 6.7 ppm and 1.2 ppm at  $-1.5$  V and  $-1.8$  V, respectively.

In the CO<sub>2</sub> reduction reaction [32,49], productions of  $C_n$  products and  $H_2$  are competitively observed. When the electrode in an aqueous electrolyte,  $H_2$  production is expected to be significant on the electrode surface via the association ( $H_{ad} + H_{ad} \rightarrow H_2$ ) of adsorbed H atoms or  $H_{ad} + H_3O^+ + e^- \rightarrow H_2 + H_2O$  [30], as observed in the present experiment. The  $H_{ad}$  is known to be formed via  $H^+ + e^- \rightarrow H_{ad}$ , where  $H_2O \rightarrow H^+ + OH^-$  [30]. CO<sub>2</sub> reduction is a multielectron process, where electrons are either provided by photogeneration or are applied by potential electrochemistry. The generally important mechanism is demonstrated below [28,45].



The production of  $C_2$  compounds requires more electrons that appear to be dependent on overlayer Cu. This needs to be studied further.

Electrochemical oxygen evolution reaction (OER) was also performed to further extend the application area of the bean sprout-like Co-TiO<sub>2</sub>/Ti nanostructures. As observed above in the electrochemical CO<sub>2</sub> reduction tests,  $H_2$  was significantly produced in the NaHCO<sub>3</sub> electrolyte media, indicating that the Co-TiO<sub>2</sub>/Ti nanostructure had a high potential applicability to water splitting. Figure 9a displays linear sweep voltammetry (LSV) curves between 1.0 V and 2.4 V (vs. RHE) in 0.1 M KOH electrolyte at a scan rate of 20 mV/s. The X-axis was rescaled from  $E_{\text{Hg/HgO}}$  using  $E_{\text{RHE}} = E_{\text{Hg/HgO}} + 0.059\text{pH} + E_{0,\text{Hg/HgO}}$ , where  $E_{\text{Hg/HgO}}$  is the measured potential and  $E_{0,\text{Hg/HgO}} = 0.098$  V [56].

For the bare Co-TiO<sub>2</sub>/Ti sample, the OER onset potential was observed at around +1.65 V (vs. RHE). The onset potential showed no significant difference, with only  $<+0.02$  V when Cu deposition was lower than 120 s. When Cu was deposited for 240 s, 480 s and 960 s, the onset potentials were observed to be +1.57 V, +1.59 V and +1.59 V (vs. RHE), respectively. These are in good agreement with the literature for ZIF-67-derivatized catalysts and Co (and/or Ni) oxide-based catalysts [13,28]. On the basis of the onset potentials ( $E_{\text{RHE}}$ ) from the LSV curves (Figure 9a), the OER overpotential ( $\eta$ ) was calculated using  $\eta = E_{\text{RHE}} - 1.23$  V [11]. The onset overpotential was then calculated to be between 340 mV and 430 mV.

The Tafel plot was obtained using the equation:  $\eta = a + b \log A$ , where  $\eta$  is the overpotential,  $a$  is the intercept,  $b$  is the Tafel slope and  $A$  is the current density ( $\text{mA}/\text{cm}^2$ ). As shown in Figure 9b, the Tafel slopes were estimated to be 124.2 mV/dec and 117.7 mV/dec for bare and 240 s Cu-deposited Co-TiO<sub>2</sub>/Ti nanostructures, respectively. When the Cu was deposited for 240 s, the OER performance was observed to be further enhanced.

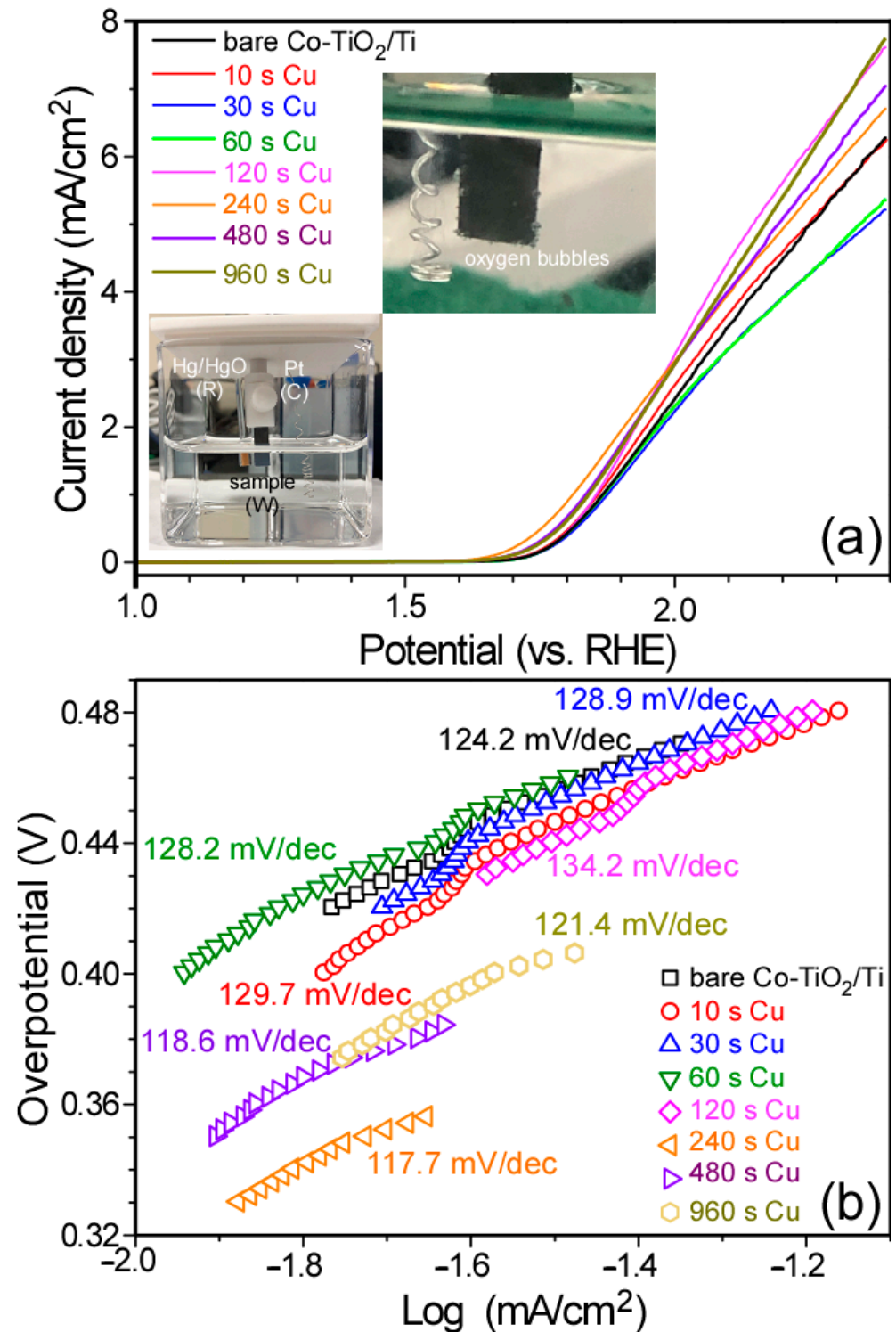


**Figure 9.** Linear sweep voltammetry profiles (a) for bare Co-TiO<sub>2</sub>/Ti and 10s, 30 s, 60 s, 120 s, 240 s, 480 s and 960 s-Cu-deposited Co-TiO<sub>2</sub>/Ti samples and the corresponding Tafel plots (b). Inset photos show the electrochemical cell with the three electrodes and oxygen bubbles on a catalyst surface.

In the OER, the Co oxide head in the bean sprout-like structure may play a more important role in enhancing activity, as based on the literature and the findings of the present study [15,18,20,28]. The overall OER is written as  $M + 4OH^- \rightarrow M + O_2(g) + 2H_2O + 4e^-$  [28]. The elementary reactions are included below and the scheme is depicted in Figure 10. All these OER processes appeared to occur more efficiently on the Co oxide head. The detailed roles of the Co oxide head and TiO<sub>2</sub> stem need to be investigated further.

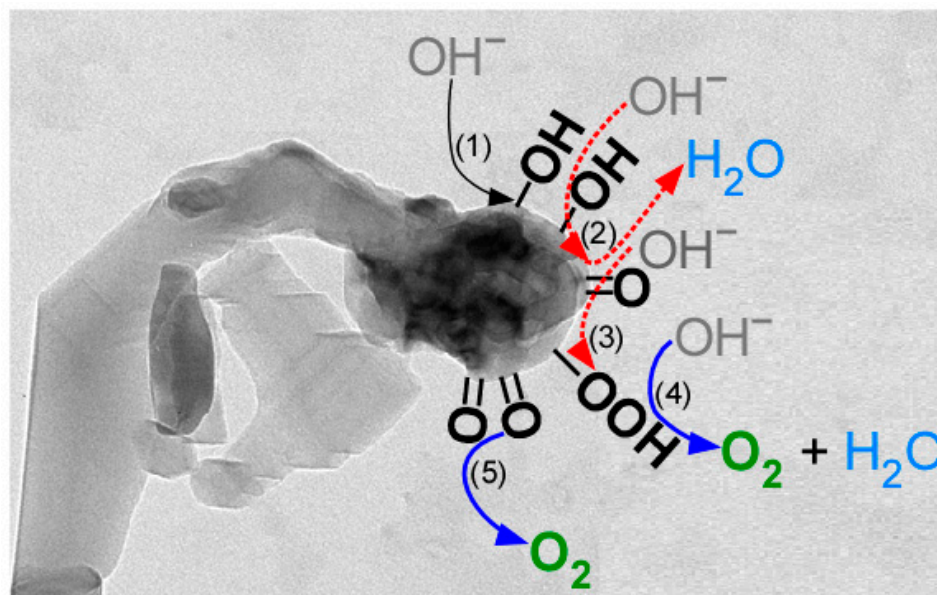
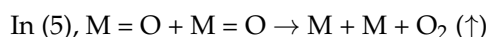
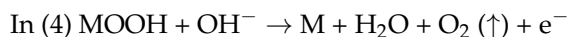
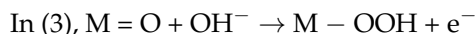
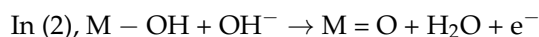
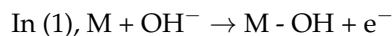


**Figure 10.** OER mechanism occurring on the Co oxide head in the bean sprout-like Co-TiO<sub>2</sub>/Ti nanostructures.

#### 4. Conclusions

In summary, we have synthesized bean sprout-like Co-TiO<sub>2</sub>/Ti nanostructures using sacrificial ZIF-67 templated on Ti sheets by thermal treatment at 800 °C under Ar-flow conditions. The physicochemical properties of the newly synthesized nanostructures were examined by X-ray diffraction analysis, scanning electron microscopy, high-resolution electron microscopy, Raman spectroscopy, energy-dispersive X-ray spectroscopy and X-ray photoelectron spectroscopy. On the basis of the results, the head and the stem were observed to be Co<sub>3</sub>O<sub>4</sub> and rutile TiO<sub>2</sub>, respectively. The interface of Ti support and TiO<sub>2</sub> appeared to form a Ti<sub>3</sub>O crystal phase. Photocatalytic and electrochemical CO<sub>2</sub> reduction experiments were demonstrated, as well as electrochemical OER for bare and Cu-deposited Co-TiO<sub>2</sub>/Ti nanostructures. The catalytic performances were observed to be dependent on the Cu deposition amount. In the photocatalytic CO<sub>2</sub> reduction, GC confirmed that CH<sub>3</sub>OH, CO and CH<sub>4</sub> were major products, with yields of 45–86 μmol/mol, 24–37 μmol/mol and 7–11 μmol/mol, respectively. Minor C<sub>2</sub> compounds of C<sub>2</sub>H<sub>2</sub>, C<sub>2</sub>H<sub>4</sub> and C<sub>2</sub>H<sub>6</sub> were meaningfully detected under 5 μmol/mol. The highest selectivity of 64% for photocatalytic MeOH production was achieved for 60 s-Cu-deposited Co-TiO<sub>2</sub>/Ti sample. For electrocatalytic CO<sub>2</sub> reduction, CO, CH<sub>4</sub> and C<sub>2</sub>H<sub>4</sub> were meaningfully produced under



50  $\mu\text{mol/mol}$ , but  $\text{H}_2$  was dominantly produced with 6000 to 16,000  $\mu\text{mol/mol}$ . The bean sprout-like Co-TiO<sub>2</sub>/Ti nanostructures were observed to show high OER performances with onset overpotentials of 330–430 mV (vs. RHE), Tafel slopes of 117–134 mV/dec and the highest performance at Cu deposition for 240 s. The present demonstration tests using ZIF-67 as a sacrificial template on metallic Ti sheet provide valuable information about the synthesis of new nanostructures, as well as potential applications regarding CO<sub>2</sub> reduction and OER for energy and the environmental management.

**Supplementary Materials:** The following are available online at <https://www.mdpi.com/article/10.3390/nano11081904/s1>, Figure S1: XPS profiles, Figure S2: Photocatalytic CO<sub>2</sub> reduction selectivities, Figure S3: Electrocatalytic CO<sub>2</sub> reduction selectivities, Figure S4: Electrochemical CO<sub>2</sub> reduction product yields.

**Author Contributions:** H.J.J. performed materials synthesis and CO<sub>2</sub> reduction; S.J.P. performed XPS; J.H.Y. performed HRTEM; S.-M.H. performed EDXS; C.K.R. designed the experimental concepts; Y.S. designed the experiments and wrote the paper. All authors have read and agreed to the published version of the manuscript.

**Funding:** This research was supported by a National Research Foundation of Korea (NRF) grant funded by the Korean government (MEST) (2016R1D1A3B04930123 and 2021R1A2C2003929).

**Data Availability Statement:** The data presented in this study are available in the article and Supplementary Material.

**Conflicts of Interest:** The authors declare no conflict of interest.

## References

1. Duan, C.; Zhang, Y.; Li, J.; Kang, L.; Xie, Y.; Qiao, W.; Zhu, C.; Luo, H. Rapid Room-Temperature Preparation of Hierarchically Porous Metal–Organic Frameworks for Efficient Uranium Removal from Aqueous Solutions. *Nanomaterials* **2020**, *10*, 1539. [[CrossRef](#)]
2. Ryu, U.; Jee, S.; Rao, P.C.; Shin, J.; Ko, C.; Yoon, M.; Park, K.S.; Choi, K.M. Recent Advances in Process Engineering and Upcoming Applications of Metal-Organic Frameworks. *Coord. Chem. Rev.* **2021**, *426*, 213544. [[CrossRef](#)]
3. Shellaiah, M.; Sun, K.-W. Progress in Metal-Organic Frameworks Facilitated Mercury Detection and Removal. *Chemosensors* **2021**, *9*, 101. [[CrossRef](#)]
4. Tang, H.; Li, W.; Jiang, H.; Lin, R.; Wang, Z.; Wu, J.; He, G.; Shearing, P.R.; Brett, D.J.L. ZIF-8-Derived Hollow Carbon for Efficient Adsorption of Antibiotics. *Nanomaterials* **2019**, *9*, 117. [[CrossRef](#)] [[PubMed](#)]
5. Zhao, H.; Wang, Y.; Zhao, L. Magnetic Nanocomposites Derived from Hollow ZIF-67 and Core-Shell ZIF-67@ZIF-8: Synthesis, Properties, and Adsorption of Rhodamine B. *Eur. J. Inorg. Chem.* **2017**, *35*, 4110–4116. [[CrossRef](#)]
6. Sun, W.; Thummavichai, K.; Chen, D.; Lei, Y.; Pan, H.; Song, T.; Wang, N.; Zhu, Y. Co-Zeolitic Imidazolate Framework@Cellulose Aerogels from Sugarcane Bagasse for Activating Peroxymonosulfate to Degrade P-Nitrophenol. *Polymers* **2021**, *13*, 739. [[CrossRef](#)] [[PubMed](#)]
7. Ethiraj, J.; Palla, S.; Reinsch, H. Insights into High Pressure Gas Adsorption Properties of ZIF-67: Experimental and Theoretical studies. *Microporous Mesoporous Mater.* **2020**, *294*, 109867. [[CrossRef](#)]
8. Song, E.; Moon, J.; Lee, J.Y.; Lee, C.O.; Chi, W.S.; Park, J.T. High-voltage solar energy conversion based on ZIF-67-derived binary redox-quasi-solid-state electrolyte. *J. Electroanal. Chem.* **2021**, *893*, 115264. [[CrossRef](#)]
9. Yu, Y.; You, S.; Du, J.; Zhang, P.; Dai, Y.; Liu, M.; Jiang, B.; Ren, N.; Zou, J. Ti<sup>3+</sup>-self-doped TiO<sub>2</sub> with multiple crystal-phases anchored on acid-pickled ZIF-67-derived Co<sub>3</sub>O<sub>4</sub>@ N-doped graphitized-carbon as a durable catalyst for oxygen reduction in alkaline and acid media. *Chem. Eng. J.* **2021**, *403*, 126441. [[CrossRef](#)]
10. Chang, P.-H.; Lee, Y.-T.; Peng, C.-H. Synthesis and Characterization of Hybrid Metal Zeolitic Imidazolate Framework Membrane for Efficient H<sub>2</sub>/CO<sub>2</sub> Gas Separation. *Materials* **2020**, *13*, 5009. [[CrossRef](#)]
11. Shaikh, Z.A.; Laghari, A.A.; Litvishko, O.; Litvishko, V.; Kalmykova, T.; Meynkhhard, A. Liquid-Phase Deposition Synthesis of ZIF-67-Derived Synthesis of Co<sub>3</sub>O<sub>4</sub>@TiO<sub>2</sub> Composite for Efficient Electrochemical Water Splitting. *Metals* **2021**, *11*, 420. [[CrossRef](#)]
12. Salahuddin, U.; Iqbal, N.; Noor, T.; Hanif, S.; Ejaz, H.; Zaman, N.; Ahmed, S. ZIF-67 Derived MnO<sub>2</sub> Doped Electrocatalyst for Oxygen Reduction Reaction. *Catalysts* **2021**, *11*, 92. [[CrossRef](#)]
13. Zhou, H.; Zheng, M.; Tang, H.; Xu, B.; Tang, Y.; Pang, H. Amorphous Intermediate Derivative from ZIF-67 and Its Outstanding Electrocatalytic Activity. *Small* **2019**, *16*, 1904252. [[CrossRef](#)]
14. Dong, Z.; Zhao, J.; Tian, Y.; Zhang, B.; Wu, Y. Preparation and Performances of ZIF-67-Derived FeCo Bimetallic Catalysts for CO<sub>2</sub> Hydrogenation to Light Olefins. *Catalysts* **2020**, *10*, 455. [[CrossRef](#)]
15. Wen, Y.; Wei, Z.; Ma, C.; Xing, X.; Li, Z.; Luo, D. MXene Boosted CoNi-ZIF-67 as Highly Efficient Electrocatalysts for Oxygen Evolution. *Nanomaterials* **2019**, *9*, 775. [[CrossRef](#)] [[PubMed](#)]

16. Yang, S.; An, X.; Qian, X. Integrated Conductive Hybrid Electrode Materials Based on PPy@ZIF-67-Derived Oxyhydroxide@CFs Composites for Energy Storage. *Polymers* **2021**, *13*, 1082. [[CrossRef](#)] [[PubMed](#)]
17. Fan, X.; Ohlckers, P.; Chen, X. Tunable Synthesis of Hollow Co<sub>3</sub>O<sub>4</sub> Nanoboxes and Their Application in Supercapacitors. *Appl. Sci.* **2020**, *10*, 1208. [[CrossRef](#)]
18. Liu, X.; Liu, H.; He, G.; Zhu, Y.; Xiao, J.; Han, L. Borate Anion Dopant Inducing Oxygen Vacancies over Co<sub>3</sub>O<sub>4</sub> Nanocages for Enhanced Oxygen Evolution. *Catalysts* **2021**, *11*, 659. [[CrossRef](#)]
19. Wang, D.; Li, S.; Du, Y.; Wu, X.; Chen, Y. Self-Templating Synthesis of 3D Hierarchical NiCo<sub>2</sub>O<sub>4</sub>@NiO Nanocage from Hydrotalcites for Toluene Oxidation. *Catalysts* **2019**, *9*, 352. [[CrossRef](#)]
20. Qi, H.; Guan, X.; Lei, G.; Zhao, M.; He, H.; Li, K.; Zhang, G.; Zhang, F.; Fan, X.; Peng, W.; et al. Bimetallic ZIF-Derived Co/N-Codoped Porous Carbon Supported Ruthenium Catalysts for Highly Efficient Hydrogen Evolution Reaction. *Nanomaterials* **2021**, *11*, 1228. [[CrossRef](#)]
21. Li, Y.; Xia, Y.; Liu, K.; Ye, K.; Wang, Q.; Zhang, S.; Huang, Y.; Liu, H. Constructing Fe-MOF-Derived Z-Scheme Photocatalysts with Enhanced Charge Transport: Nanointerface and Carbon Sheath Synergistic Effect. *ACS Appl. Mater. Interfaces* **2020**, *12*, 25494–25502. [[CrossRef](#)] [[PubMed](#)]
22. Yang, F.; Xiong, T.; Huang, P.; Zhou, S.; Tan, Q.; Yang, H.; Huang, Y.; Balogun, M.-S. Nanostructured Transition Metal Compounds Coated 3D Porous Core-Shell Carbon Fiber as Monolith Water Splitting Electrocatalysts: A General Strategy. *Chem. Eng. J.* **2021**, *423*, 130279. [[CrossRef](#)]
23. Zhang, J.; Huang, Y.; Lu, X.; Yang, J.; Tong, Y. Enhanced BiVO<sub>4</sub> Photoanode Photoelectrochemical Performance via Borate Treatment and a NiFeO<sub>x</sub> Cocatalyst. *ACS Sustain. Chem. Eng.* **2021**, *9*, 8306–8314. [[CrossRef](#)]
24. Lu, X.; Ye, K.; Zhang, S.; Zhang, J.; Yang, J.; Huang, Y.; Ji, H. Amorphous Type FeOOH Modified Defective BiVO<sub>4</sub> Photoanodes for Photoelectrochemical Water Oxidation. *Chem. Eng. J.* **2021**, *428*, 131027. [[CrossRef](#)]
25. Yuan, X.; Mu, Q.; Xue, S.; Su, Y.; Zhu, Y.; Sun, H.; Deng, Z.; Peng, Y. Polypyrrole Reinforced ZIF-67 with Modulated Facet Exposure and Billion-fold Electrical Conductivity Enhancement towards Robust Photocatalytic CO<sub>2</sub> Reduction. *J. Energy Chem.* **2021**, *60*, 202–208. [[CrossRef](#)]
26. Becerra, J.; Nguyen, D.-T.; Gopalakrishnan, V.-N.; Do, T.-O. Plasmonic Au Nanoparticles Incorporated in the Zeolitic Imidazolate Framework (ZIF-67) for the Efficient Sunlight-Driven Photoreduction of CO<sub>2</sub>. *ACS Appl. Energy Mater.* **2020**, *3*, 7659–7665. [[CrossRef](#)]
27. Peng, H.J.; Zhu, L.; Wang, Y.L.; Chao, H.Y.; Jiang, L.; Qiao, Z.P. CdS/ZIF-67 Nanocomposites with Enhanced Performance for Visible Light CO<sub>2</sub> Photoreduction. *Inorg. Chem. Commun.* **2020**, *117*, 107943–107947. [[CrossRef](#)]
28. Park, H.; Park, B.H.; Choi, J.; Kim, S.; Kim, T.; Youn, Y.-S.; Son, N.; Kim, J.H.; Kang, M. Enhanced Electrochemical Properties and OER Performances by Cu Substitution in NiCo<sub>2</sub>O<sub>4</sub> Spinel Structure. *Nanomaterials* **2020**, *10*, 1727. [[CrossRef](#)] [[PubMed](#)]
29. Xing, C.; Zhang, Y.; Liu, Y.; Wang, X.; Li, J.; Martinez-Alanis, P.R.; Spadaro, M.C.; Guardia, P.; Arbiol, J.; Llorca, J.; et al. Photodehydrogenation of Ethanol over Cu<sub>2</sub>O/TiO<sub>2</sub> Heterostructures. *Nanomaterials* **2021**, *11*, 1399. [[CrossRef](#)] [[PubMed](#)]
30. Yang, J.H.; Park, S.J.; Rhee, C.K.; Sohn, Y. Photocatalytic CO<sub>2</sub> Reduction and Electrocatalytic H<sub>2</sub> Evolution over Pt(0,II,IV)-Loaded Oxidized Ti Sheets. *Nanomaterials* **2020**, *10*, 1909. [[CrossRef](#)] [[PubMed](#)]
31. Zhang, H.; Tang, Q.; Li, Q.; Song, Q.; Wu, H.; Mao, N. Enhanced Photocatalytic Properties of PET Filaments Coated with Ag-N Co-Doped TiO<sub>2</sub> Nanoparticles Sensitized with Disperse Blue Dyes. *Nanomaterials* **2020**, *10*, 987. [[CrossRef](#)] [[PubMed](#)]
32. Sohn, Y.; Huang, W.; Taghipour, F. Recent Progress and Perspectives in the Photocatalytic CO<sub>2</sub> Reduction of Ti-Oxide-Based Nanomaterials. *Appl. Surf. Sci.* **2017**, *396*, 1696–1711. [[CrossRef](#)]
33. Momma, K.; Izumi, F. VESTA 3 for Three-Dimensional Visualization of Crystal, Volumetric and Morphology Data. *J. Appl. Crystallogr.* **2011**, *44*, 1272–1276. [[CrossRef](#)]
34. Bibi, S.; Pervaiz, E.; Yang, M.; Rabi, O. MOF Embedded and Cu Doped CeO<sub>2</sub> Nanostructures as Efficient Catalyst for Adipic Acid Production: Green Catalysis. *Catalysts* **2021**, *11*, 304. [[CrossRef](#)]
35. Sochacka, P.; Jurczyk, M.U.; Kowalski, K.; Wirstlein, P.K.; Jurczyk, M. Ultrafine-Grained Ti-31Mo-Type Composites with HA and Ag, Ta<sub>2</sub>O<sub>5</sub> or CeO<sub>2</sub> Addition for Implant Applications. *Materials* **2021**, *14*, 644. [[CrossRef](#)] [[PubMed](#)]
36. Gong, Y.; Wang, Y.; Sun, G.; Jia, T.; Jia, L.; Zhang, F.; Lin, L.; Zhang, B.; Cao, J.; Zhang, Z. Carbon Nitride Decorated Ball-Flower like Co<sub>3</sub>O<sub>4</sub> Hybrid Composite: Hydrothermal Synthesis and Ethanol Gas Sensing Application. *Nanomaterials* **2018**, *8*, 132. [[CrossRef](#)] [[PubMed](#)]
37. Huyen, T.T.T.; Chi, T.T.K.; Dung, N.D.; Kosslick, H.; Liem, N.Q. Enhanced Photocatalytic Activity of {110}-Faceted TiO<sub>2</sub> Rutile Nanorods in the Photodegradation of Hazardous Pharmaceuticals. *Nanomaterials* **2018**, *8*, 276. [[CrossRef](#)]
38. NIST DTSA-II Software. Available online: <https://cstl.nist.gov/div837/837.02/epq/dtsa2/> (accessed on 1 May 2021).
39. Sundriyal, S.; Shrivastav, V.; Mishra, S.; Deep, A. Enhanced Electrochemical Performance of Nickel Intercalated ZIF-67/rGO Composite Electrode for Solid-State Supercapacitors. *Int. J. Energy Res.* **2020**, *45*, 30859–30869.
40. Shi, X.; Zhang, Y.; Liu, X.; Jin, H.; Lv, H.; He, S.; Hao, H.; Li, C. A Mild in-Situ Method to Construct Fe-Doped Cauliflower-Like Rutile TiO<sub>2</sub> Photocatalysts for Degradation of Organic Dye in Wastewater. *Catalysts* **2019**, *9*, 426. [[CrossRef](#)]
41. Challagulla, S.; Tarafder, K.; Ganesan, R.; Roy, S. Structure Sensitive Photocatalytic Reduction of Nitroarenes over TiO<sub>2</sub>. *Scientific Rep.* **2017**, *7*, 1–11.
42. Wójcik, S.; Grzybek, G.; Stelmachowski, P.; Sojka, Z.; Kotarba, A. Bulk, Surface and Interface Promotion of Co<sub>3</sub>O<sub>4</sub> for the Low-Temperature N<sub>2</sub>O Decomposition Catalysis. *Catalysts* **2020**, *10*, 41. [[CrossRef](#)]

43. Gwag, J.S.; Sohn, Y. Interfacial Natures and Controlling Morphology of Co Oxide Nanocrystal Structures by Adding Spectator Ni Ions. *Bull. Korean Chem. Soc.* **2012**, *33*, 505–510. [[CrossRef](#)]
44. Tsai, C.-H.; Fei, P.-H.; Lin, C.-M.; Shiu, S.-L. CuO and CuO/Graphene Nanostructured Thin Films as Counter Electrodes for Pt-Free Dye-Sensitized Solar Cells. *Coatings* **2018**, *8*, 21. [[CrossRef](#)]
45. Muthukrishnaraj, A.; Al-Zahrani, S.A.; Al Otaibi, A.; Kalaivani, S.S.; Manikandan, A.; Balasubramanian, N.; Bilgrami, A.L.; Ahamed, M.A.R.; Khan, A.; Asiri, A.M.; et al. Enhanced Photocatalytic Activity of Cu<sub>2</sub>O Cabbage/RGO Nanocomposites under Visible Light Irradiation. *Polymers* **2021**, *13*, 1712. [[CrossRef](#)]
46. Naumkin, A.V.; Kraut-Vass, A.; Gaarenstroom, S.W.; Powell, C.J. NIST Standard Reference Database 20, Version 4.1. 2012. Available online: <https://srdata.nist.gov/xps/> (accessed on 5 June 2021).
47. Sohn, Y.; Pradhan, D.; Zhao, L.; Leung, K.T. Anomalous Oxidation Resistance of “Core-Only” Copper Nanoparticles Electrochemically Grown on Gold Nanoislands Prefunctionalized by 1,4-Phenylene Diisocyanide. *Electrochem. Solid-State Lett.* **2012**, *15*, K35–K39. [[CrossRef](#)]
48. Yoon, H.J.; Yang, J.H.; Park, S.J.; Sohn, Y. Thermal CO Oxidation and Photocatalytic CO<sub>2</sub> Reduction over Bare and M-Al<sub>2</sub>O<sub>3</sub> (M = Co, Ni, Cu, Rh, Pd, Ag, Ir, Pt, and Au) Cotton-Like Nanosheets. *Nanomaterials* **2021**, *11*, 1278. [[CrossRef](#)]
49. Ali, S.; Flores, M.C.; Razzaq, A.; Sorcar, S.; Hiragond, C.B.; Kim, H.R.; Park, Y.H.; Hwang, Y.; Kim, H.S.; Kim, H.; et al. Gas Phase Photocatalytic CO<sub>2</sub> Reduction, “A Brief Overview for Benchmarking”. *Catalysts* **2019**, *9*, 727. [[CrossRef](#)]
50. Jang, H.J.; Park, S.J.; Yang, J.H.; Hong, S.-M.; Rhee, C.K.; Kim, D.; Sohn, Y. Photocatalytic and Photoelectrocatalytic Properties of Eu(III)-Doped Perovskite SrTiO<sub>3</sub> Nanoparticles with Dopant Level Approaches. *Mater. Sci. Semicond. Process.* **2021**, *132*, 105919. [[CrossRef](#)]
51. Yoon, H.J.; Yang, J.H.; Park, S.J.; Rhee, C.K.; Sohn, Y. Photocatalytic CO<sub>2</sub> Reduction and Hydrogen Production over Pt/Zn-Embedded β-Ga<sub>2</sub>O<sub>3</sub> Nanorods. *Appl. Surf. Sci.* **2021**, *536*, 147753. [[CrossRef](#)]
52. Choi, Y.I.; Yang, J.H.; Park, S.J.; Sohn, Y. Energy Storage and CO<sub>2</sub> Reduction Performances of Co/Co<sub>2</sub>C/C Prepared by an Anaerobic Ethanol Oxidation Reaction Using Sacrificial SnO<sub>2</sub>. *Catalysts* **2020**, *10*, 1116. [[CrossRef](#)]
53. Lin, J.; Sun, X.; Qin, B.; Yu, T. Improving the photocatalytic reduction of CO<sub>2</sub> to CO for TiO<sub>2</sub> hollow spheres through hybridization with a cobalt complex. *RSC Adv.* **2018**, *8*, 20543–20548. [[CrossRef](#)]
54. Hong, S.; Rhee, C.K.; Sohn, Y. Photoelectrochemical Hydrogen Evolution and CO<sub>2</sub> Reduction over MoS<sub>2</sub>/Si and MoSe<sub>2</sub>/Si Nanostructures by Combined Photoelectrochemical Deposition and Rapid-Thermal Annealing Process. *Catalysts* **2019**, *9*, 494. [[CrossRef](#)]
55. Lee, H.I.; Yu, H.; Rhee, C.K.; Sohn, Y. Electrochemical Hydrogen Evolution and CO<sub>2</sub> Reduction over Hierarchical MoS<sub>x</sub>Se<sub>2-x</sub> Hybrid Nanostructures. *Appl. Surf. Sci.* **2019**, *489*, 976–982. [[CrossRef](#)]
56. Liu, X.J.; Liu, H.X.; Peng, X.Y.; Qi, G.C.; Luo, J. Porous Mn-Doped FeP/Co<sub>3</sub>(PO<sub>4</sub>)<sub>2</sub> Nanosheet Arrays as an Efficient Electrocatalyst for pH-Universal Overall Water Splitting. *ChemSusChem* **2019**, *12*, 1334. [[CrossRef](#)] [[PubMed](#)]